Applied Energy 272 (2020) 115236

Contents lists available at ScienceDirect

Applied Energy

journal homepage: www.elsevier.com/locate/apenergy

Barium aluminate improved iron ore for the chemical looping combustion of syngas

Haiming Wang[a,*], Xiaomin Dou[a], Andrei Veksha[a], Wen Liu[a,b], Apostolos Giannis[c], Liya Ge[a], Teik Thye Lim[a,d], Grzegorz Lisak[a,d,*]

[a] Residues and Resource Reclamation Centre, Nanyang Environment and Water Research Institute, Nanyang Technological University, Singapore 637141, Singapore
[b] School of Chemical and Biomedical Engineering, Nanyang Technological University, Singapore 637459, Singapore
[c] School of Environmental Engineering, Technical University of Crete (TUC), University Campus, 73100 Chania, Greece
[d] School of Civil and Environmental Engineering, Nanyang Technological University, Singapore 639798, Singapore

HIGHLIGHTS

- Chemical looping combustion was applied for the treatment of MSW syngas.
- $BaAl_2O_4$ greatly improved the reactivity of iron ore as the oxygen carrier.
- Lattice oxygen activity was enhanced due to the increased oxygen vacancies.
- Interaction between $BaAl_2O_4$ and iron ore gave rise to highly porous morphology.

ARTICLE INFO

Keywords:
Chemical looping combustion
Oxygen carrier
$BaAl_2O_4$
Oxygen vacancies
MSW syngas

ABSTRACT

Chemical looping combustion (CLC), as an advanced combustion technology, has attracted much attention because of its applicability to a variety of fuels and its ability to achieve inherent carbon capture. However, CLC of municipal solid waste (MSW) has been seldom reported. In this study, we investigated the CLC of simulated MSW-derived syngas using iron ore (IO)-based oxygen carriers (OCs). To enhance the redox activity of the IO, barium aluminate ($BaAl_2O_4$) was used for the first time as a promoter of the OC. It was found that the surface decoration with $BaAl_2O_4$ significantly improved the redox performance of IO over the temperature range of 700–900 °C. Almost 100% syngas combustion over 30 redox cycles was achieved by IO modified with 10% of $BaAl_2O_4$ (IO-10BA) at a space velocity of 31700 h^{-1}, whereas only ~70% combustion efficiency was achieved by pristine IO. Additionally, $BaAl_2O_4$ doping improved the oxygen transport capacity of the IO by 36.2%. Based on complementary characterization analyses, we found that more oxygen vacancies were formed in the modified OC due to the oxygen non-stoichiometry nature of the $BaAl_2O_4$ and its interaction with the iron oxide species. This interaction facilitated the rapid migration of the lattice oxygen in the bulk phase, thereby enhancing the reactivity and increasing the oxygen transport capacity of the OCs. The addition of $BaAl_2O_4$ also induced a change to the solid morphology, making the OC become more porous over redox cycles, a phenomenon that was partly responsible for the high combustion performance of the IO-10BA.

1. Introduction

Chemical looping combustion (CLC) has been investigated extensively in the last two decades as an energy-efficient carbon capture technology, which addresses the excessive CO_2 emissions to the atmosphere [1,2], especially those generated by the combustion of fossil fuels [3]. CLC consists of two steps, namely oxygen carriers (OCs) supported combustion process in the Fuel Reactor (FR) and OCs regeneration process in the Air Reactor (AR). Direct contact between the fuel and the air is avoided in FR. As such, it does not require downstream gas–gas separation of the flue gas for carbon capture which often incurs intensive energy input. Typically, when metal oxides are used as the OCs, the lattice oxygen of which facilitates the complete combustion of fuel in the FR, producing a fairly pure stream with CO_2 as the main component, ready for compression and further utilization.

A variety of fuels such as natural gas [4], syngas [5], coal [6], and

* Corresponding authors.
E-mail addresses: wanghaiming89@gmail.com (H. Wang), g.lisak@ntu.edu.sg (G. Lisak).

https://doi.org/10.1016/j.apenergy.2020.115236
Received 3 February 2020; Received in revised form 28 April 2020; Accepted 17 May 2020
Available online 05 June 2020

biomass [7] have been studied in chemical looping processes. However, the application of CLC to municipal solid waste (MSW) utilization to achieve waste-to-energy (WtE) conversion, simultaneous carbon capture, and pollutant reduction has been rarely reported [8]. Recently, advanced thermochemical MSW conversion processes, such as pyrolysis and gasification for the generation of syngas, have attracted widespread attention. Compared with conventional incineration, pyrolysis and gasification show great potentials in inhibiting the formation of dioxins and furans [9,10]. More importantly, the generated syngas can be utilized in advanced combustion systems to achieve higher energy efficiency with lower carbon footprint per unit electricity generated. Nevertheless, the high concentrations of impurities in the MSW syngas, such as HCl, H_2S, and alkali chlorides still limit the efficient utilization of the generated MSW syngas [11,12], owing to the need for syngas purification by low temperature gas scrubbing systems [13,14].

Because of its ability to combust the fuel in the absence of air, CLC presents an attractive solution to address the challenges arising from the impurities in the raw MSW syngas. CLC is usually operated in the temperature range of 800–1200 °C, which is similar to the operation temperature range of MSW gasifiers [9]. Therefore, the generated raw MSW syngas can be directly introduced to the FR for combustion with minimal energy penalty. Simultaneously, the hot air generated by the exothermic AR is free of contaminants, and thus is suitable for effective heat exchange to raise the pressure of generated steam for efficient power generation. As a result, CLC can achieve simultaneous flue gas combustion for power generation and carbon capture. The potential adverse effect of the syngas impurities on the performance of OCs can be avoided through the screening of suitable OCs, which is the key to efficient CLC performance [15]. The potential redox active OCs include the oxides of Ni, Mn, Cu, Co– and Fe, etc. [2]. Amongst the oxides, NiO has been proven to have high reactivity, especially for methane combustion. However, Ni is more expensive than other metal oxides and is both toxic and carcinogenic [1]. Mn- and Cu-based OCs have higher oxygen transport capacity than Fe-based OCs, but they are susceptible to H_2S attack, forming metal sulfides [16], which may cause the deactivation of the OCs during the long term cyclic operation. Another concern with Cu-based OCs is their tendency for melting due to the low melting point of Cu [17]. There are few reports on the development of Co-based OCs [1], partially because of their serious environmental issues, as well as low equilibrium conversion of H_2 (~95–97%) and CO (~87–97%) by the CoO/Co redox couple over the temperature range of 800–1200 °C (Figure S1 in supporting information).

Among suitable OCs, Fe-based materials are considered as a promising candidate for large-scale implementation, because of their abundant natural source, low cost, thermal stability, and environmental friendliness. More importantly, the reaction between the iron oxides and impurity HCl is thermodynamically unfavorable, as shown in Figure S2. In addition, it was found that the presence of H_2S did not have any adverse effects [18] and may even improve [19,20] the stability and capability of the iron oxides over redox cycles.

The use of unmodified natural iron ores for CLC has been investigated in both batch [21–23] and continuous fluidized bed reactors [24,25]. In general, the reactivity of the IO is relatively low compared to synthetic materials because of their low surface area and porosity [26,27]. To improve the reactivity and the regenerability of the IO particles, a number of dopants, e.g. Mn_2O_3 [26], NiO [28], and CuO [29,30] were used as promoters. However, these dopants are more sensitive to the presence of impurities than iron oxides, thus limiting their application in combusting MSW syngas. Alkali or alkaline earth metals including K [31] and Ca [32], which are not redox active themselves, were also used as promoters to decorate iron ores. In fact, these alkaline materials are often used as adsorbents for acid gases [33,34], thus the in situ purification of flue gas can be realized during the CLC process.

In the present study, IO is chosen as the basis for developing OCs for the CLC of syngas derived from MSW. To improve the redox performance of natural IO for CLC of the syngas, barium aluminate ($BaAl_2O_4$) was investigated as a dopant to promote the activity of the OC. $BaAl_2O_4$, which belongs to the family of stuffed tridymites, was reported to have a high melting point (1815 °C) [35,36] that may benefit the cyclic stability of the OCs. Additionally, the structure of $BaAl_2O_4$ can accommodate high concentration of oxygen defects [37], which could potentially benefit redox kinetics by enhancing oxygen ion diffusivity [38]. These properties make $BaAl_2O_4$ an attractive material for chemical looping processes. To our best knowledge, this is the first report of using $BaAl_2O_4$ as a dopant to the material formulation for the development of highly efficient OCs.

2. Experimental

2.1. Preparation of oxygen carriers

Commercially available IO from China (imported by SG Labware, Singapore) was used as the base material for the preparation of the OC. Barium aluminate with a purity higher than 99% was purchased from Alfa Aesar (US) and used without any further purification. The $BaAl_2O_4$ was loaded on the surface of the IO by wet-mixing. In a typical preparation, 10 to 40 g (depending on the desired mass ratio of $BaAl_2O_4$ to IO) of $BaAl_2O_4$ was added into 100 mL deionized (DI) water under stirring (500 rpm). Then, 200 g of IO, crushed and sieved to the size range of 150–250 μm, was added to the $BaAl_2O_4$ suspension. The resulting mixture was heated at 70 °C until most of the water evaporated. The slurry was transferred to a crucible and dried at 105 °C overnight, followed by calcination at 950 °C for 5 hr in air. The obtained fresh OC composites were sieved again to the size range of 150–250 μm. The OCs with $BaAl_2O_4$ to IO mass ratios of 0:100, 5:100, 10:100, and 20:100 were prepared and labelled as IO, IO-5BA, IO-10BA, and IO-20BA, respectively. Table 1 lists the composition of the IO before and after $BaAl_2O_4$ loading, as measured by X-ray fluorescence (XRF). The XRF analysis shows that the unmodified IO contains more than 85% of Fe_2O_3.

2.2. Characterization of oxygen carriers

The OCs before and after redox cycles were characterized by complementary techniques to explore possible underlying mechanisms that resulted in the change in the performance of oxygen carrier after $BaAl_2O_4$ doping. The composition of the OCs was analyzed by XRF (PANalytical, Netherlands). X-ray powder diffraction (XRD) was used to determine the crystal phase change of the OCs. The XRD analyses were conducted using a XRD-6000 diffractometer (Shimadzu) with Cu-Kα radiation in continuous scan mode with a step size of 0.02° in the 2θ range of 15° to 90°. X-ray photoelectron spectroscopy (XPS) was carried out on an AXIS Supra (Kratos), with monochromatic radiation from Al/Ag Kα source, to identify the surface composition and the oxidation state of the various metal elements. The binding energy of C1s, which is fixed at 284.8 eV, was taken as an internal calibration standard for all

Table 1
Main composition of IO before and after loading with $BaAl_2O_4$ given by XRF.

Oxides	IO (wt%)	IO-5BA (wt%)	IO-10BA (wt%)	IO-20BA (wt%)
Fe_2O_3	85.45	72.83	69.67	68.04
SiO_2	6.52	5.93	5.89	3.76
TiO_2	3.54	3.35	3.36	2.92
MgO	0.61	0.46	0.42	0.32
CaO	0.94	0.93	0.91	0.70
Al_2O_3	1.71	10.18	11.96	12.84
BaO	–	4.96	6.49	10.34
Others	1.23	1.36	1.30	1.08
$BaAl_2O_4$*	–	8.36	10.81	17.22

* Calculated based on the content of BaO.

tests. The morphology and surface elemental mapping of the OCs were characterized by field emission scanning electron microscope with energy dispersive spectroscopy (FESEM-EDS, JSM-7200F, JEOL). To identify the particle bulk morphology, cross sections of the OCs before and after redox reactions were examined by FESEM. Briefly, the OC particles were embedded in epoxy resin at room temperature. Sandpaper (P1200, 3 M) was then used for the initial polishing of the epoxy resin bed. A cross section polisher (SM-9020CP, JEOL) was finally applied to further fine-polish the particles cross section using an argon ion beam. The Brunauer–Emmett–Teller (BET) surface area and total pore volume of the OCs were analyzed based on the nitrogen adsorption–desorption isotherms measured at 77 K on a Quadrasorb SI (Quantachrome Instrument).

2.3. H_2-TPR and TGA operation

Hydrogen temperature programmed reduction (H_2-TPR) was performed on Autochem 2910 (Micromeritics, US) to evaluate the activities of the lattice oxygen in the fresh and the used OCs. In a typical H_2-TPR, the OC powder (about 35 mg) was first degassed at 150 °C in N_2 for 1 h, followed by naturally cooling to room temperature. After the degassing, the OC particles were heated to 950 °C at a rate of 10 °C/min in 50 mL/min of 5 vol% H_2/N_2. The H_2 composition in the outlet was quantified by a thermal conductivity detector.

The oxygen transport capacities of the fresh and used OCs were quantified by isothermal reduction–oxidation experiments carried out in TGA (STA 449 F3 Jupiter, NETZSCH) at 900 °C. During the redox cycle, the mass change of the OCs was measured with a precision of 0.1 μg. In each test, 17 vol% CO/N_2 was used as the fuel to reduce the OC for 60 min. After purging with N_2 for 10 min, the reduced sample was oxidized in air for 20 min. The gas flow rate was controlled at 340 mL/min by mass flow controllers. The amount of sample used in each test was approximately 20 mg. The mass loss, X (wt%), of the OCs during the redox reaction in TGA can be calculated as:

$$X = \frac{m_0 - m_t}{m_0} \times 100\% \quad (1)$$

where m_0 and m_t are the masses (mg) of the OCs at their fully oxidized state and at time t during the isothermal redox stage, respectively.

The mass loss rate, x (%/min), was calculated as:

$$x = \frac{dX}{dt} \quad (2)$$

The oxygen transport capacity, R (wt%), was calculated based on the mass loss at the end of the 60 min reduction (in 17 vol% CO/N_2) in the TGA:

$$R = \frac{m_o - m_r}{m_o} \times 100\% \quad (3)$$

where m_r is the mass (mg) of the OCs by the end of the isothermal reduction stage.

2.4. Redox performance tests

The redox performance of the OCs was tested in a batch fluidized bed (bFB) reactor as shown in Fig. 1. The reactor was a quartz tube with an inner diameter of 15 mm. It was heated by an electrical furnace to the desired temperature (700–900 °C). In the middle of the quartz tube, a fritted silica disc was used as a sample holder as well as a gas distributor. Two type K thermocouples, 10 mm above and below the fritted quartz disc, respectively, were used to monitor the temperature inside the reactor. A simulated MSW syngas consisting of ~ 10 vol% CO, ~10 vol% H_2, ~5 vol% CO_2, and 25 vol% H_2O, with N_2 balance, was used as the reduction gas. This composition was based on a previous study [14]. Steam was generated by injecting water into the reactor feed using a syringe pump with an infusion rate of 0.1 mL/min. To avoid water condensation, all the pipelines were heated to 150 °C. 8 vol % O_2 in N_2 was used as the oxidizing gas. In each redox cycle, the syngas was introduced into the reactor for 5 min. After purging with N_2 for 3 min, the OC was regenerated in the oxidizing gas for 10 min. At all stages of a redox experiment, the total inlet gas flowrate was maintained at 500 sccm (standard cubic centimeters per minute), which corresponds to 3.8 times the minimum fluidization velocity at 900 °C. For consistency, the amount of IO used in each test was the same, i.e. 10 g, and without any diluting sand. The OC bed height was 23–27 mm when unfluidized. The superficial gas residence time was about 0.12 s. For each test, 20 to 50 redox cycles were performed. The syngas before and after the reaction was collected in gas bags for off-line analysis by a gas chromatograph equipped with thermal conductivity and flame ionization detectors (GC-TCD-FID, 7390B, Agilent). The concentration of steam was calculated based on a hydrogen balance. For the 1st, 10th, and 20th reduction cycle, the flue gas was sampled every minute. For other cycles, the average of the flue gas composition over every 5 min interval was sampled and analyzed. Each test was duplicated to validate the repeatability of the results.

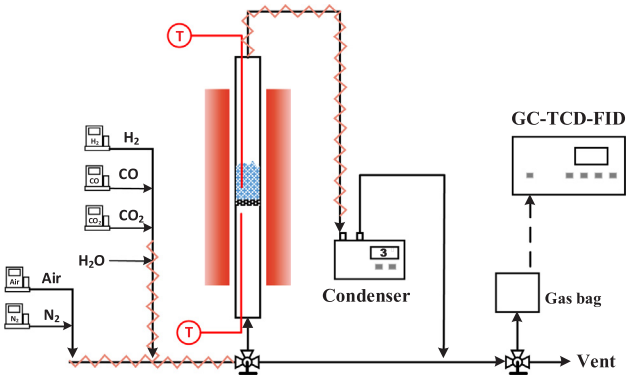

Fig. 1. Schematic diagram of bFB experimental setup.

Based on the analyzed gas compositions, the combustion efficiencies of CO and H_2, respectively, were calculated based on a nitrogen balance:

$$\eta_{H_2} = 1 - \frac{y_{H_2}}{y_{H_2,in}} \times \frac{y_{N_2,in}}{y_{N_2}} \quad (4)$$

$$\eta_{CO} = 1 - \frac{y_{CO}}{y_{CO,in}} \times \frac{y_{N_2,in}}{y_{N_2}} \quad (5)$$

where η_i is the combustion efficiency for species i; y_i is the molar fraction of species i as measured by GC-TCD-FID; the subscript in indicates the inlet molar concentration.

The actual amount of lattice oxygen transported per unit mass of OCs in each cycle was defined as:

$$\Omega = \frac{\int_0^{5\ \mathrm{min}} (\eta_{H_2} Y_{H_2,in} + \eta_{CO} Y_{CO,in}) \times 16 dt}{m} \quad (6)$$

where Ω is the transported lattice oxygen ratio of the OCs; $Y_{H2,in}$ *and* $Y_{CO,in}$ are the input mole flow rates of H_2 and CO, respectively, in [mol/min]; m is the mass of the OC used in the fluidized bed at its fully oxidized state, in [g].

3. Results and discussion

3.1. Redox tests in a batch fluidized bed

3.1.1. Redox performance of the OCs

The typical profiles of the combustion efficiencies, viz. $\eta_{H_2}$and η_{CO}, during reduction, and gaseous oxygen concentration in the outlet during oxidation are shown in Fig. 2. The combustion efficiency of

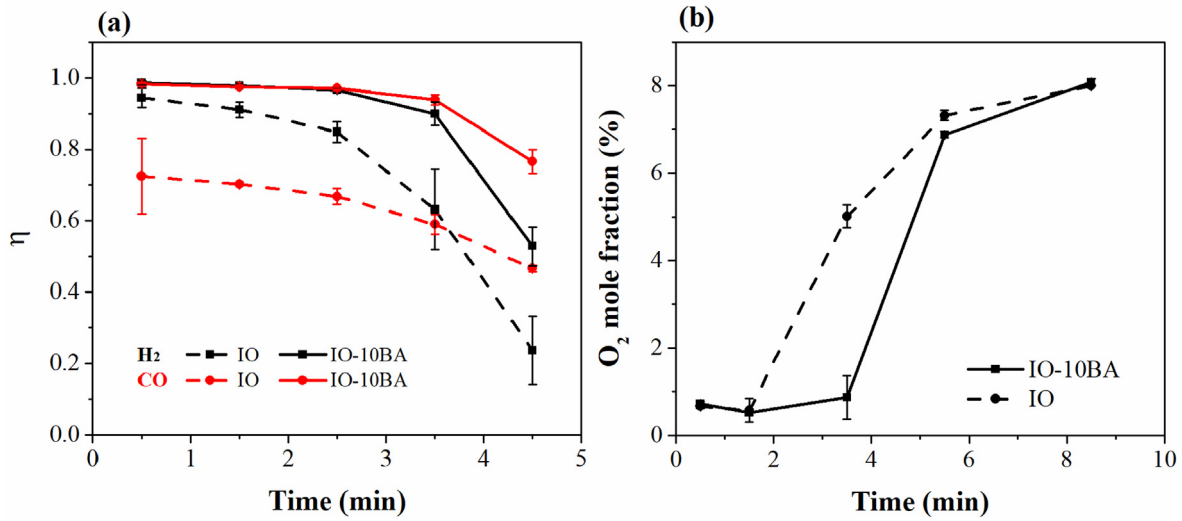

Fig. 2. Variation of (a) combustion efficiency, and (b) oxygen content against reaction time in 10th redox cycle at the reaction temperature of 900 °C.

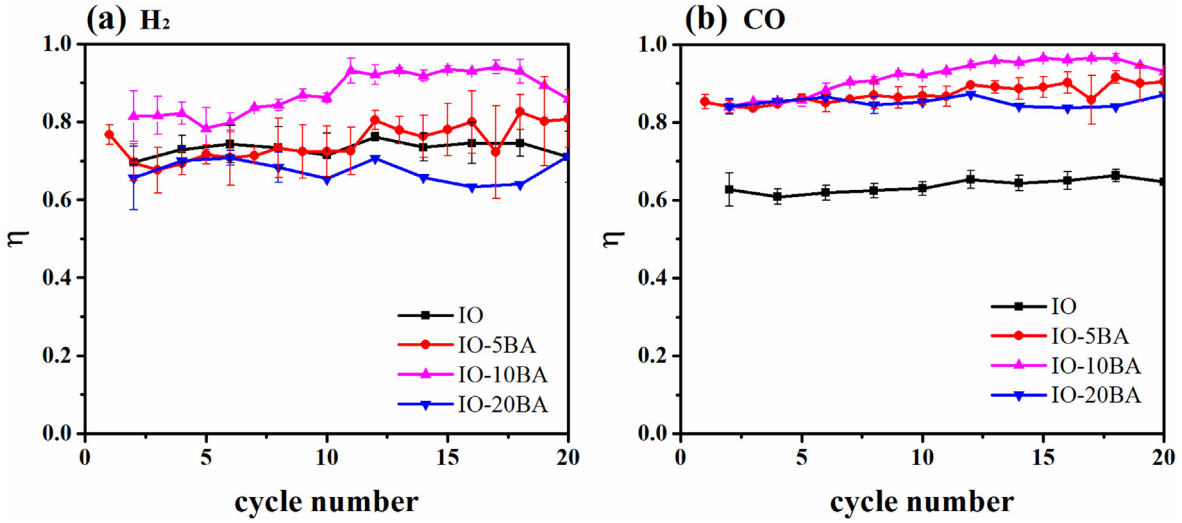

Fig. 3. Combustion efficiency for (a) H_2 and (b) CO with IO modified by different contents of barium aluminate at the temperature of 900 °C.

unmodified IO was generally lower compared to that of IO-10BA, especially in the case of η_{CO}, which decreased from ~ 0.7 to 0.5 within the first 5 min of reduction, as shown in Fig. 2 (a). With 10% $BaAl_2O_4$ doping, the combustion efficiencies of both CO and H_2 remained > 0.95 during the first 3 min. As the Fe_2O_3 was gradually converted to Fe_3O_4, the combustion efficiency decreased as a result of the reduced lattice oxygen activity in Fe_3O_4–FeO/Fe compared to that in Fe_2O_3–Fe_3O_4. In general, the reactivity of the OC with H_2 was higher than that with CO, which is in agreement with a previous study [39]. On the other hand, η_{H_2} dropped off much faster between 2.5 and 5 min than η_{CO}. This can be explained by the water–gas shift (WGS) reaction, which is catalyzed by Fe_3O_4 [40], consuming CO whilst generating additional H_2 (see R1).

$$H_2O(g) + CO(g) = H_2(g) + CO_2(g) \quad \text{(R1)}$$

The effect of WGS was more clearly shown by the η_{CO} and η_{H_2}profiles in Figure S3. For IO, η_{H_2}decreased from 94% to 24% over the 5 min reduction at 900 °C (Figure S3 (a)). At 800 °C, some H_2 was generated during the last minute of the reduction, resulting in negativeη_{H_2}, as shown in Figure S3 (b). At 700 °C, about 50% more H_2 was generated by WGS (Figure S3 (c)), whilst the onset of negative η_{H_2} was much earlier in each cycle than the case at 800 °C. The rapid drop in $\eta_{H_2}$with time was accompanied by the steady consumption of CO due to the WGS. In fact, by comparing the measured composition at the reactor outlet with the equilibrium composition (shown in Figure S3 (d)) calculated based on Eq (7):

$$K = \frac{[CO_2][H_2]}{[CO][H_2O]} \quad (7)$$

it can be seen that chemical equilibria have been reached towards the end of the reduction stage at both 800 and 700 °C. In the presence of $BaAl_2O_4$, the onset of significant WGS was postponed, as shown in Figure S3 (b) and (c), causing η_{H_2} to be much higher.

Fig. 2 (b) shows the variation in the mole fraction of oxygen during the oxidation process of the 10th cycle. The rate of oxidation was faster than that of reduction for both IO and IO-10BA, showing complete oxygen uptake by the reduced OCs during the first several minutes (as will also be evidenced by the TGA test in the following section). From Fig. 2 (b), it can be seen that the oxygen breakthrough for IO-10BA was delayed compared to IO, suggesting higher lattice oxygen activity in the $BaAl_2O_4$ modified sample. Following breakthrough, the oxygen concentration quickly recovered to the inlet concentration level. Therefore, the 10 min duration is sufficient for completely regenerating the lattice oxygen in the OCs. In the following sections, the discussion will be primarily focused on the reduction of the OCs.

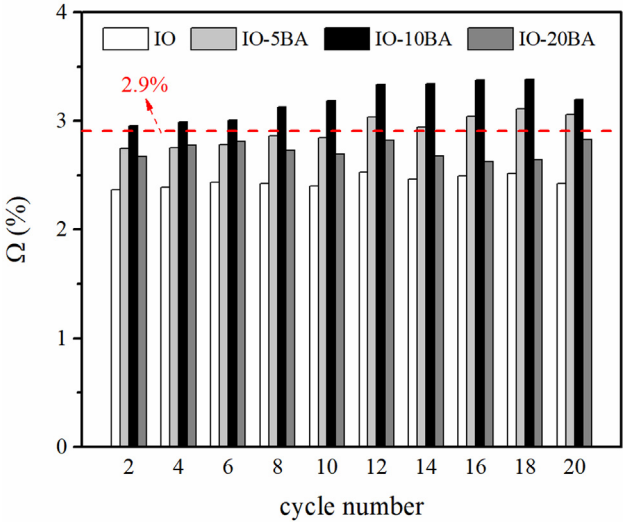

Fig. 4. Oxygen transport ability, Ω, of different OCs within 20 cycles at the temperature of 900 °C.

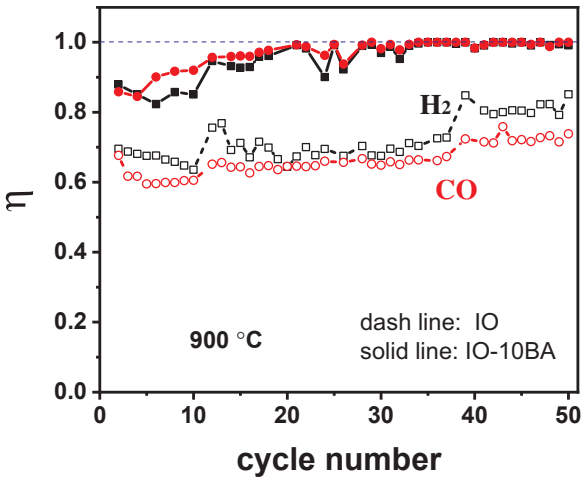

Fig. 6. Combustion efficiency for 50 cycles at the temperature of 900 °C.

3.1.2. *Effect of $BaAl_2O_4$ loading*

The combustion efficiencies of the simulated syngas with IO modified by 5%, 10%, and 20% of $BaAl_2O_4$ are shown in Fig. 3. For unmodified IO, the average η_{H_2} over 20 cycles was 0.73. No obvious improvement was observed after loading with 5% $BaAl_2O_4$. With 20% of $BaAl_2O_4$, the η_{H_2} even dropped to 0.68, possibly owing to the

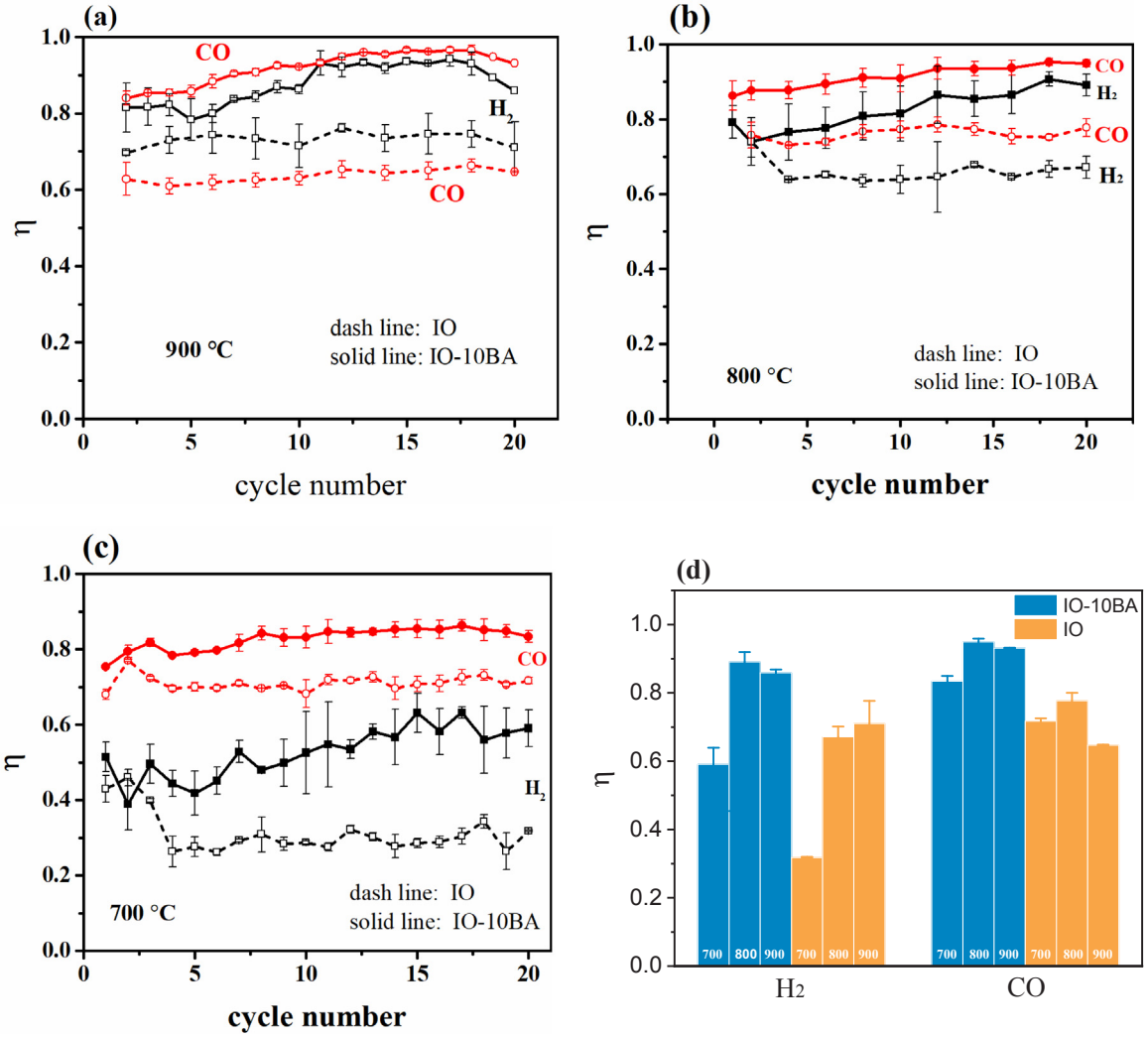

Fig. 5. Combustion efficiency for H_2 and CO with IO modified by 10% of $BaAl_2O_4$ at different temperatures. (a) 700 °C; (b) 800 °C; (c) 900 °C; (d) combustion efficiency of the 20th cycle at different temperatures. The error bars represent the standard error.

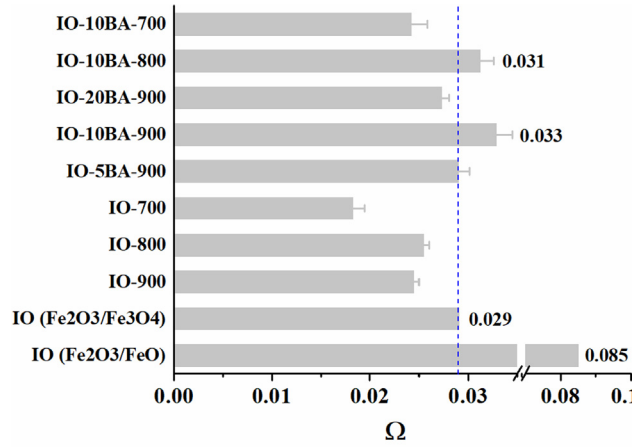

Fig. 7. Average oxygen transport ability, Ω, of 20 redox cycles for different OCs at different temperatures. (For IO-900 and IO-10BA-900, the average was taken for 50 cycles).

Fig. 8. Volume variation of the OCs after 50 cycles of redox reaction.

coverage of the active Fe_2O_3 by $BaAl_2O_4$, hindering the contact between H_2 and IO. IO-10BA showed a distinct improvement compared to other OCs, with η_{H_2}reaching up to 0.94 after 10 cycles. The addition of $BaAl_2O_4$ rendered even more improvement to η_{CO}. For the first several cycles, η_{CO} increased from ~0.62 for IO to ~0.85 for the IO-10BA, the performance of which continued to improve after 5 cycles, with η_{CO} exceeding 0.95 after 12 cycles. For all OCs, η_{CO}increased slightly with the cycle number, suggesting some kind of activation process during the redox experiments [41]. Furthermore, the addition of 10% $BaAl_2O_4$ not only improved the combustion efficiency remarkably, but also accelerated the activation process.

The actual amount of lattice oxygen transported per unit mass of OC in each cycle, Ω, is shown in Fig. 4. For IO (containing 85.45% Fe_2O_3), the theoretical lattice oxygen transport capacities for the Fe_2O_3/Fe_3O_4 and Fe_2O_3/FeO redox couples are 2.9% and 8.5%, respectively. Thermodynamically, only the Fe_2O_3/Fe_3O_4 redox couple could facilitate complete combustion. Indeed, for unmodified IO, the lattice oxygen transported per cycle was consistently below 2.4%, i.e. about 83% of the available lattice oxygen (for the Fe_2O_3/Fe_3O_4 conversion) was consumed during the 5-min syngas combustion in each cycle. Similar to the combustion efficiencies, the amount of lattice oxygen consumed also increased slightly with redox cycles. The doping of $BaAl_2O_4$ significantly enhanced the Ω, especially in the cases of IO-5BA and IO-10BA. For IO-10BA, Ω over 20 cycles was between 3.1% and 3.5%, consistently higher than the maximum capacity of the Fe_2O_3/Fe_3O_4 redox couple, but lower than 8.5% for Fe_2O_3/FeO. The above results suggest that the addition of $BaAl_2O_4$ not only accelerates the redox reactions, but also promotes the reducibility of Fe_2O_3.

3.1.3. Stability of the modified iron ore at different temperatures

Fig. 5 shows the combustion efficiencies of CO and H_2 by IO and IO-10BA at different temperatures. It can be seen that the addition of $BaAl_2O_4$ significantly improved both η_{CO} and η_{H_2}at all temperatures tested. At 900 °C (Fig. 5(a)), the addition of $BaAl_2O_4$ increased the average η_{CO} and η_{H_2} by 28.3% and 14.4%, respectively. Furthermore, the reactivity of IO-10BA increased gradually over the redox cycles, suggesting an apparent activation process, which is also observed in Figs. 3 and 4. At the lower temperatures of 800 and 700 °C, η_{H_2} values are accordingly lower. At 700 °C (Fig. 5(c)), the average H_2 combustion efficiency in IO was only ~30%, which is much lower than the ~70% measured at 900 °C. In IO-10BA, the H_2 combustion efficiency varied between 40% and 60% at 700 °C, also much lower than the ~90% as observed at 900 °C. The trend of variation of η_{CO} with temperature was different from that of η_{H_2}. Fig. 5(d) summarizes the combustion efficiencies at the 20th cycle measured at different temperatures. η_{CO} appeared less temperature-dependent than η_{H_2}. In general, η_{CO}remained at relatively high levels for different operation temperatures. For IO-10BA, η_{CO} decreased slightly from 94% (900 °C) to 83% (700 °C), whilst for IO, η_{CO} was even slightly higher at lower reaction temperatures. The variation of the apparent combustion efficiencies with temperature can be explained by the fact that WGS is favored at low temperatures. As mentioned above, CO can be consumed by WGS at low temperatures resulting in the η_{CO} to remain high.

The stability of IO and IO-10BA was further evaluated by conducting 50 redox cycles at 900 °C. The results of the 50 cycles are presented in Fig. 6. For IO, $\eta_{H_2}$and η_{CO} increased gradually from 70% and 68% at the 1st cycle to 85% and 74% at the 50th cycle, respectively. IO-10BA showed better long term performance, achieving almost complete combustion of both H_2 and CO from the 30th cycle onwards.

The average amounts of lattice oxygen transported by all the OCs, measured at different temperatures, are shown in Fig. 7. The theoretical oxygen transport capacity for unmodified IO is also indicated for comparison. Under all testing conditions, the OCs modified with $BaAl_2O_4$ exhibited greater oxygen transport ability than the unmodified IO. 10% $BaAl_2O_4$ loading showed the best performance (i.e. higher reactivity and stability) at 800 and 900 °C. The enhanced oxygen transport capacity will be further discussed in the sections below.

3.2. Characterization of OCs and the enhancement mechanism

3.2.1. Morphology change of the OCs before and after redox cycles

Interestingly, it was found that the total volume of the OCs increased significantly after 50 cycles, as shown in Fig. 8, with the bed height for IO and IO-10BA expanding by 1.9 and 2.5 times, respectively.

Table 2
Bed height, surface area and pore volume of the OCs before and after redox cycles.

Samples	Before reaction			After 50 cycles		
	Bed height (mm)	BET surface area (m^2/g)	Total pore volume (cm^3/kg)	Bed height (mm)	BET surface area (m^2/g)	Total pore volume (cm^3/kg)
IO	23	0.21	0.56	43	0.25	0.68
IO-10BA	26	0.40	0.76	64	0.94	1.30

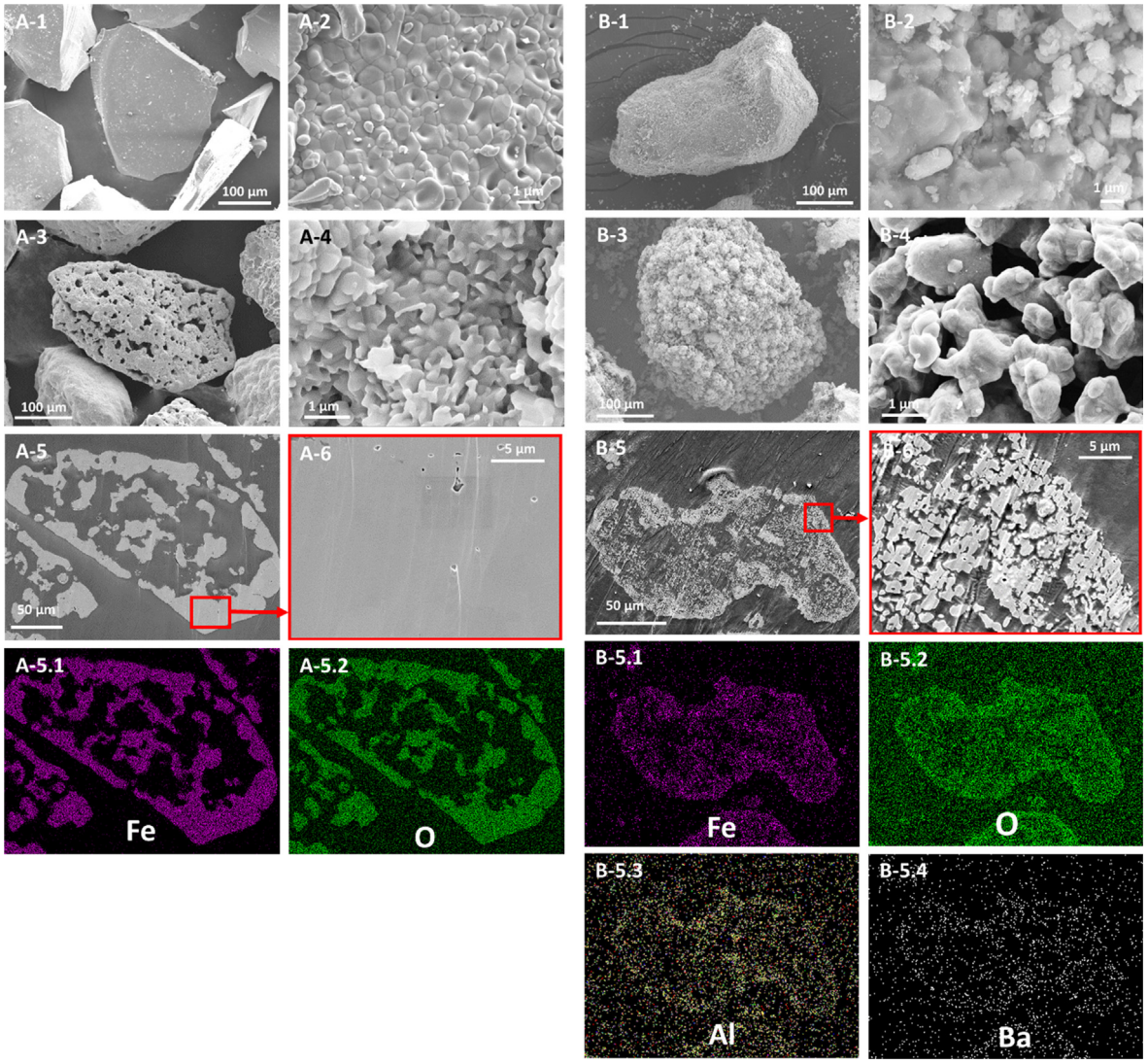

Fig. 9. FESEM-EDS images of OCs before and after 50 redox cycles. A1-A2: fresh IO; A3-A6: IO after 50 cycles; A5.1-A5.2: elements mappings for A5; B1-B2: fresh IO-10BA; B3-B6: IO-10BA after 50 cycles; B5.1-B5.4: elements mappings for B5. The cross section morphology of the IO is shown in A-5 and A-6; the cross section morphology of the IO-10BA is shown in B-5 and B-6.

The OC particles became more porous after the redox cycles, especially in the case of IO-10BA. The surface area and pore volume for the IO and IO-10BA before and after 50 cycles are listed in Table 2. For the fresh OCs, the BET specific surface area and total pore volume of the OCs increased slightly after loading with 10 wt% of $BaAl_2O_4$. After 50 cycles, the surface area of the spent IO-10BA increased to 0.94 m^2/g, about 3.7 times that of the spent IO. The addition of $BaAl_2O_4$ also increased the pore volume of the spent OC from 0.68 to 1.30 cm^3/kg.

This pore generation phenomenon was further examined by FESEM. The surface morphology changes of the IO and IO-10BA before and after 50 redox cycles are shown in Fig. 9. It can be seen that the fresh IO particles were non-porous materials with a dense surface structure. The morphology of the fresh IO featured the structure of small cells (Fig. 9 A-2). The non-porous structure caused the small surface area of the materials as shown in Table 2. After modification, it was found that $BaAl_2O_4$ with the size of 1–2 μm was uniformly distributed on the surface of the IO (B-1 and B-2). To distinguish the loaded $BaAl_2O_4$ from the IO, a selected surface of the IO-10BA was scanned by EDS, with the resulting element mapping shown in Figure S4. It may be the case that the doping of small grains of $BaAl_2O_4$ caused the increases in the surface area and the pore volume observed in Table 2.

Different from the smooth and dense surface of the fresh IO, macropores emerged on the surface after 50 redox cycles (A-3). The generation of the additional macroporosity, which facilitated better access for syngas to react with the interior of the OC particles, may be a factor enabling the activation of the IO over redox cycles. Apart from the macropores, the surface texture of the cycled IO (A-4) also became slightly more porous than that of the fresh sample (A-2). The cross section of a cycled IO particle, shown in A-5, depicts the formation of large cavities inside the particle, encapsulated by a dense shell that was decorated with macropores.

With the loading of 10% $BaAl_2O_4$, the morphology of IO-10BA changed significantly after 50 cycles. Uniformly distributed macropores with size of several microns were formed on the surface of IO-10BA as shown in Fig. 9 B-3 and B-4. The surface became highly porous after 50 cycles (B-4), contrasting the dense surface for spent IO particles (A-4). The cross-sectional morphology of the IO-10BA is depicted in B-5, which shows cavities with a variety of sizes inside the OC particle. Different from the cross section of IO, in which large lumps were observed inside the bulk (A-5), clusters of small grains dominate the interior of the IO-10BA particle. The EDS element mappings shown in B-5.1 to B-5.4 indicate the migration of $BaAl_2O_4$ from the surface of the iron ore particles into their interior. This migration could probably facilitate and accelerate the formation of pores inside the OC particles.

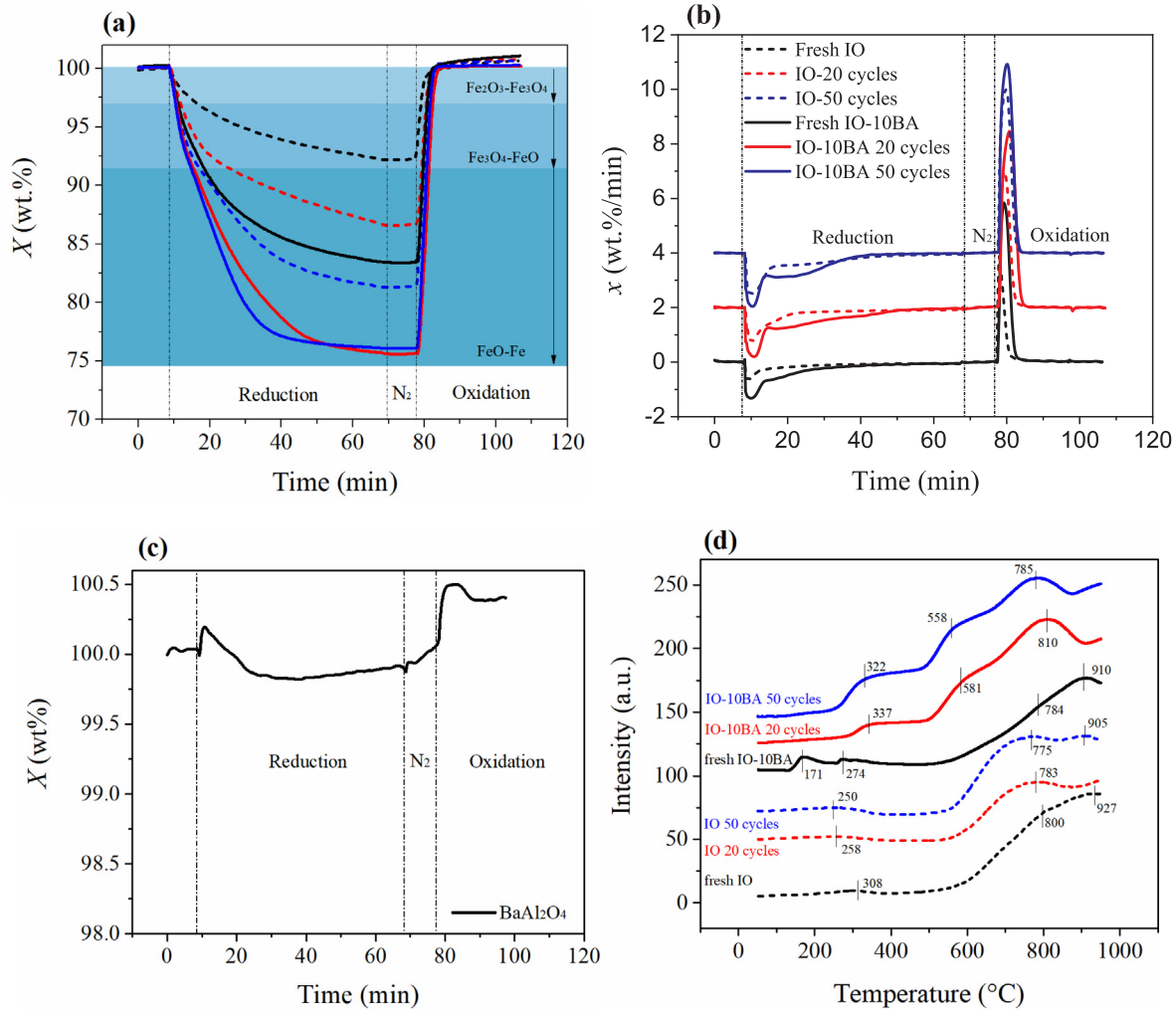

Fig. 10. TGA and H2-TPR data. (a): mass losses, *X*, and (b): mass loss rates, *x*, for IO and IO-10BA before and after redox reactions; (c): mass loss ratio of fresh $BaAl_2O_4$ powder; (d) H_2-TPR patterns.

This is discussed in detail in the Discussion section below. The results of FESEM analysis are consistent with the larger surface area and pore volume of the cycled IO-10BA. The highly porous surface and inner structure of the cycled IO-10BA greatly benefit intra-particle mass transfer, providing better contact of the gaseous reactants with OCs.

3.2.2. *Lattice oxygen transport capacity and its activity for IO-10BA*

The redox performance of the fresh and used OCs was further tested in TGA to demonstrate the effect of $BaAl_2O_4$ on the reactivity of the lattice oxygen in the IO. Fig. 10 shows the fractional mass loss and the rate of mass change of the OCs during the isothermal redox cycle at 900 ˚C. It can be seen that the addition of $BaAl_2O_4$ had significantly improved the oxygen transport capacity during the 60 min reduction in 17 vol% CO/N_2 (shown in Fig. 10 (a)), whilst the rate of reaction was enhanced 2 to 3 times, especially for the reduction from Fe_3O_4 to Fe (shown in Fig. 10 (b)).

The reduction of Fe_2O_3 in IO and IO-10BA can be divided into three stages, viz. Fe_2O_3 to Fe_3O_4, Fe_3O_4 to FeO, and FeO to Fe. Nevertheless, these three stages, especially the last two, usually overlap one another, as shown in Fig. 10 (b) and (d). Based on the elemental analysis of IO (shown in Table 1), the fractional mass loss curve can be mapped against the theoretical phase transitions, as shown in Fig. 10 (a). As $BaAl_2O_4$ was not redox active, it is anticipated that the theoretical mass loss of IO-10BA would be less than in case of IO, due to the dilution effect. In 17 vol% CO/N_2, all OCs except fresh IO could be completely reduced past Fe_3O_4 in ~ 150 s. For fresh IO, the reduction mainly achieved the conversion from Fe_2O_3 to FeO in 60 min. The observed rate of reduction of IO was the lowest, mainly because of the low porosity and reactivity of the IO. As the number of redox cycles increased in bFB, the IO particles appear to be gradually activated because of the generation of additional porosity and surface area, as clearly shown in Table 2 and Fig. 9. Thus, the IO particles taken from the bFB after 20 and 50 cycles achieved faster rates and subsequently reduction beyond FeO, i.e. final mass losses were 13.4% and 18.8% for IO after 20 cycles and 50 cycles, respectively, compared to the 7.8% for the fresh IO. With $BaAl_2O_4$, the reduction of fresh IO-10BA from Fe_2O_3 to Fe_3O_4 was almost twice as fast as that of fresh IO. The rate of the subsequent reduction stages (Fe_3O_4–FeO–Fe) was also boosted significantly. This observation is in agreement with the enhanced performance seen in Fig. 7. For IO-10BA, there was not much difference in performance between after 20 cycles and after 50 cycles, i.e. the reactivity of IO-10BA has stabilized after 20 redox cycles; this is also consistent with the bFB results shown in Fig. 6. The oxygen transport capacity reached 23.9 wt% for IO-10BA after 50 cycles, which is close to the theoretical oxygen transport capacity for IO (Fe_2O_3–Fe, 25.6 wt %). Furthermore, the oxidation rate of the reduced OCs was also improved with the addition of the $BaAl_2O_4$ as can be seen in Fig. 10 (b).

To further elucidate the role of $BaAl_2O_4$ in the redox reactions, pure $BaAl_2O_4$ was tested in TGA under the same operation condition. The normalized mass loss curve is shown in Fig. 10 (c). Upon introducing 17 vol% CO/N_2, a mass loss of ~ 0.25 wt% was observed following a small mass gain. This suggests that a small fraction of the lattice oxygen

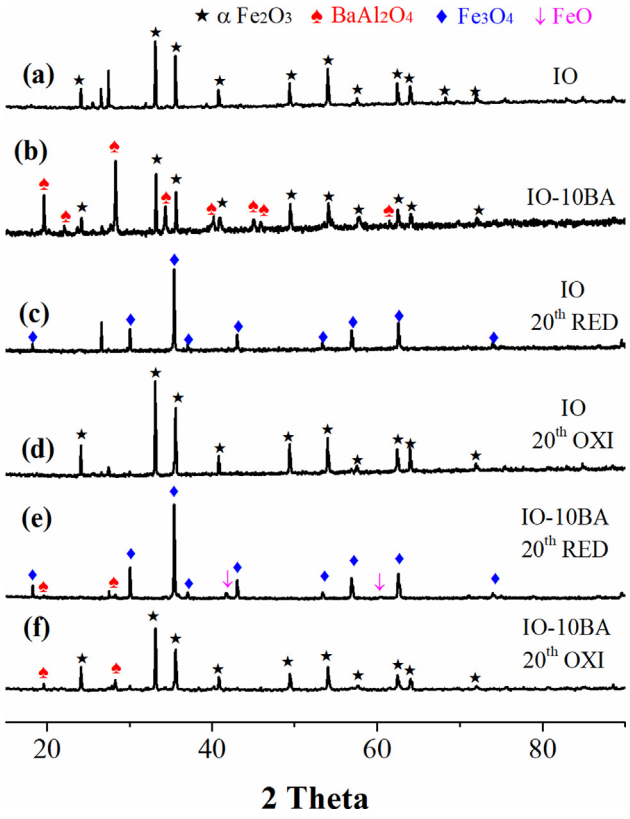

Fig. 11. XRD patterns of the OCs before and after redox reactions.

in $BaAl_2O_4$ can participate in the redox reaction using CO as a fuel. Although this mass change seems negligible compared to that of IO-10BA (shown in Fig. 10 (a)), the formation of these oxygen vacancies in $BaAl_2O_4$ under the reducing environment might facilitate the enhanced mobility of the bulk lattice oxygen in the OCs, thus improving the redox reactivity. During the oxidation stage, $BaAl_2O_4$ rapidly gained an additional mass of 0.5 wt%, which also evidenced that the $BaAl_2O_4$ can accommodate substantial oxygen non-stoichiometry during the redox cycles [35].

H_2-TPR was conducted to further examine the nature of the lattice oxygen in the OCs. Fig. 10 (d) shows the TPR profiles for IO and IO-10BA before and after redox cycles. Under identical experimental conditions, the addition of $BaAl_2O_4$ resulted in the shift of reduction peaks to lower temperatures, manifesting the improved reducibility and lattice oxygen activity. The intensity of the TCD signals for IO-10BA was also enhanced, meaning higher H_2 consumption and oxygen carrying ability than the pristine IO.

For fresh IO, two reduction peaks ranging from 600 to 950 °C are presented. The first peak around 800 °C, can be assigned to the transformation of Fe_2O_3 to Fe_3O_4. The second peak around 927 °C can be ascribed to the partial reduction of Fe_3O_4 to FeO. This is in line with the observation in TGA, where the successive reduction steps overlap with each other (Fig. 10 (b)) while only partial reduction of Fe_3O_4 to FeO was achieved at 900 °C. The weak peak at low temperature (308 °C) could be caused by surface adsorbed oxygen. After redox cycles in bFB, the TPR peaks of IO shifted to lower temperatures, revealing the increased reducibility, which is in agreement with the TGA results.

For the fresh IO-10BA, the peaks corresponding to the transformation of Fe_2O_3–Fe_3O_4 and Fe_3O_4–FeO shifted to lower temperatures of 784 and 910 °C, respectively, comparing to fresh IO. In addition, two new peaks appeared around 171 and 274 °C, which may be attributed to the release of lattice oxygen of $BaAl_2O_4$, as shown in the TGA results (Fig. 10 (c)). After the redox cycles, the disappearance of the low temperature peaks suggested the loss of $BaAl_2O_4$ from the OC surface. After 20 cycles, the Fe_2O_3–Fe_3O_4 peak of IO-10BA shifted to around 581 °C, which is much lower than that of IO. It was also observed that the Fe_3O_4 was further reduced to FeO with a major peak at 810 °C. Due to the short reaction time in TPR, the complete reduction peak of FeO–Fe after 850 °C was not observed, which was also reported previously when IO was used as OCs [28]. It is worth noting that IO-10BA after 20 cycles showed an apparent H_2 consumption peak at 337 °C, which is possibly ascribed to the formation of perovskite type iron ferrite species, e.g. $BaFeO_3$, as a result of the chemical interaction between $BaAl_2O_4$ and Fe_2O_3. This assertion is supported by a previous study, which reported a broad H_2 consumption peak between 280 and 480 °C during the H_2-TPR of $BaFeO_3$ [42], producing $Ba_2Fe_2O_5$ and H_2O [43,44]. The IO-10BA after 20 and 50 cycles showed similar TPR profiles except for a slightly shift of the reduction peak to lower temperatures from 20 cycles to 50 cycles. This is in agreement with the TGA result suggesting that the performance of IO-10BA tended to be stable after 20 cycles.

3.2.3. Phase change of the OCs

The XRD patterns of the IO and IO-10BA before and after 20 redox cycles are shown in Fig. 11. For the fresh IO, the major phase was Fe_2O_3 (hematite, JCPDS 87-1166). The unidentified peaks with 2θ in the range of 25 to 30° may come from impurities containing oxides of Si, Ti, and/or Al as suggested by the results of the XRF (Table 1) analysis. In IO-10BA, the diffraction peaks of $BaAl_2O_4$ (JCPDS 72-0387) can be clearly seen suggesting the loading of $BaAl_2O_4$ on the IO surface. For both IO and IO-10BA, the conversion of Fe_2O_3 to Fe_3O_4 (JCPDS 88-0866) can be seen after reduction. After oxidation, the reduced samples were oxidized to their initial state with Fe_2O_3 as the major phase. No obvious diffraction peaks of FeO were identified in the XRD patterns for the reduced IO, implying that the reduction of Fe_2O_3 mostly terminated at Fe_3O_4. By contrast, FeO diffraction peaks were observed for the reduced IO-10BA sample. Thus some of the Fe_3O_4 could be further reduced to FeO with the loading of $BaAl_2O_4$ during the reaction, causing the enhanced oxygen transport capacity as observed in Fig. 4 and Fig. 7. The significantly reduced intensity of the $BaAl_2O_4$ diffraction peaks after 20 cycles suggests the possible chemical interaction between $BaAl_2O_4$ and Fe_2O_3. This interaction may involve simple ionic exchanges, such as the one reported by Huang et al [45]. However, no new crystal phase was observed in the cycled OC, meaning that either the amount of new phase formed was insignificant or the new phase had low crystallinity. Nevertheless, given that the formation of barium ferrites is thermodynamically feasible [46,47], the possible interaction between iron oxides and $BaAl_2O_4$ merits further and more systematic investigations.

Fig. 12 shows the XPS spectra of Fe2p and O1s for the IO and IO-10BA before and after 20 redox cycles. The high resolution Fe 2p3/2 spectra were fitted using peaks corresponding to the Gupta and Sen (GS) multiplets [48] as shown in Fig. 12 (a). These peaks have full widths at half-maximum (FWHM) ranging from 1.0 to 1.6 eV and with a binding energy interval of ~ 1 eV. In addition to the multiplet structure, a surface peak and a satellite peak due to the shake-up or charge transfer process were also used for fitting [48]. The multiplet parameters are summarized in Table 3. For the fresh IO and IO-10BA shown in Fig. 12 (a), only the Fe^{3+}quadruplet was observed, which is consistent with the observation in the XRD patterns. After reduction process, the Fe^{2+} 2p3/2 triplet was also observed for both IO and IO-10BA. In the reduced IO, the ratio of Fe^{2+}/ Fe^{3+}, calculated from the area under the corresponding multiplets, was 0.46 (shown in Table 3), which is slightly less than the theoretical ratio for Fe_3O_4 (0.5), implying the incomplete reduction of Fe_2O_3 to Fe_3O_4 after 5 min time-on-stream; this result is in line with the low oxygen transport ability of unmodified IO, as shown in Fig. 4 and Fig. 7. In the reduced IO-10BA, a ratio Fe^{2+}/ Fe^{3+} of 0.60 was obtained (shown in Table 3), indicating that the presence of $BaAl_2O_4$ promotes the reduction of Fe^{3+} to Fe^{2+} beyond the Fe_2O_3/Fe_3O_4 redox couple. This is also in accordance with the

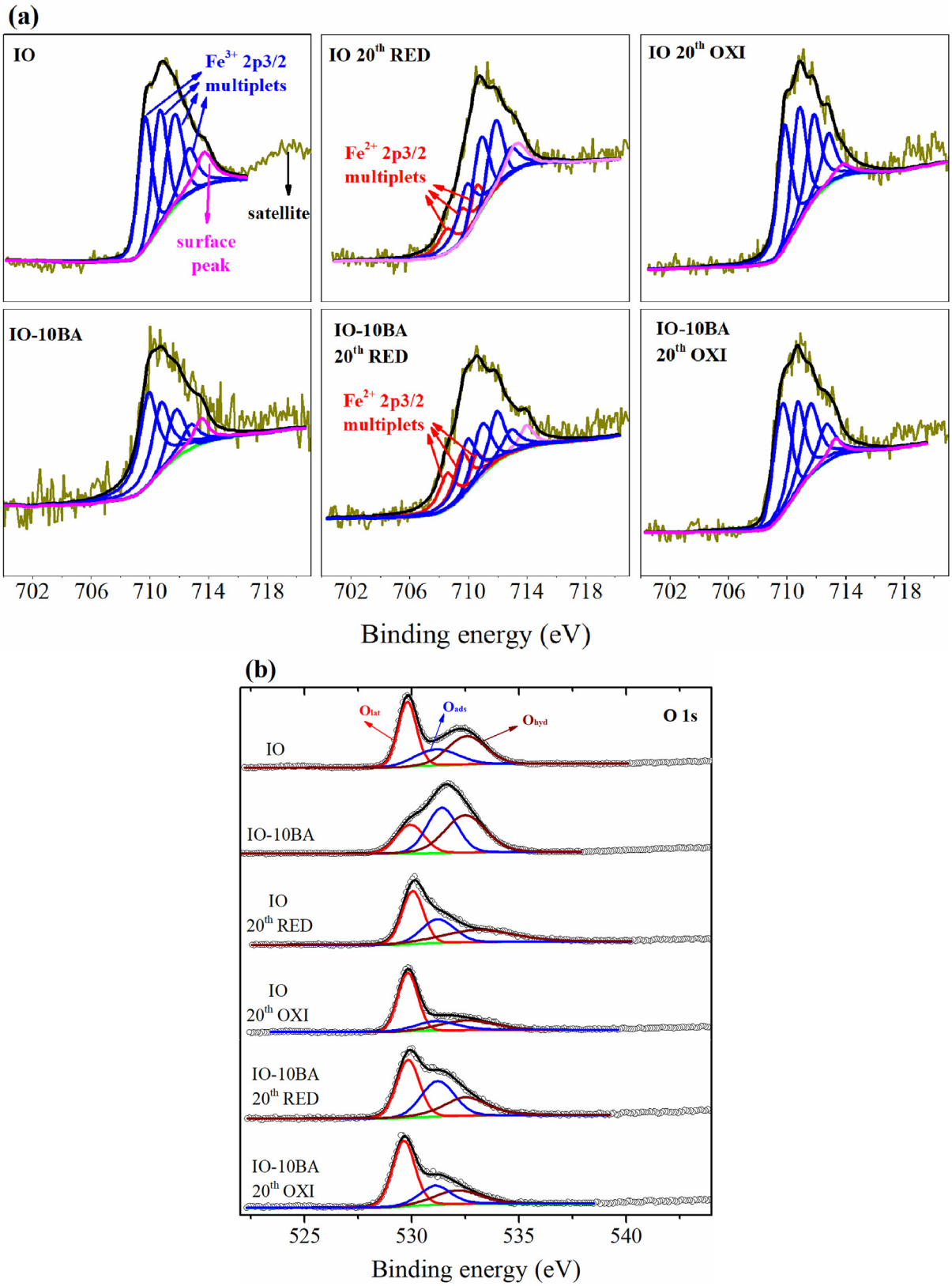

Fig. 12. XPS spectra of IO and IO-BA before and after 20 cycles (a) Fe2p, (b) O1s.

observation of FeO diffraction peaks of reduced IO-10BA shown in Fig. 11 (e).

The high resolution O 1s spectra are shown in Fig. 12 (b). The spectra can be deconvoluted to three different peaks corresponding to lattice oxygen (O_{lat}), physically adsorbed oxygen (O_{ads}), and hydroxyl oxygen (O_{hyd}) with binding energies of 529.8, 531.2, and 532.5 eV, respectively [49,50]. It is generally accepted that the surface adsorbed oxygen, O_{ads}, is mainly associated with the oxygen vacancies formed on

Table 3
Binding energy of the fitting peaks of Fe 2p3/2 spectra for IO and IO-BA*.

Samples		IO	IO-10BA	IO Red	IO Oxi	IO-10BA Red	IO-10BA Oxi
Fe^{3+} 2p3/2	Peak 1	712.7 [1.3]	712.8 [1.4]	712.8 [1.1]	712.8 [1.1]	712.9 [1.5]	712.7 [1.4]
	Peak 2	711.7 [1.4]	711.8 [1.4]	711.8 [1.0]	711.8 [1.2]	711.9 [1.3]	711.6 [1.4]
	Peak 3	710.7 [1.2]	710.8 [1.5]	710.8 [1.0]	710.8 [1.2]	710.9 [1.5]	710.7 [1.2]
	Peak 4	709.7 [1.1]	709.9 [1.5]	709.8 [1.4]	709.8 [1.1]	709.9 [1.4]	709.7 [1.4]
Fe^{2+} 2p3/2	Peak 1	–	–	710.5 [1.0]	–	710.5 [1.1]	–
	Peak 2	–	–	709.5 [1.4]	–	709.5 [1.3]	–
	Peak 3	–	–	708.5 [1.4]	–	708.5 [1.4]	–
Fe^{2+}/Fe^{3+}		–	–	0.46	–	0.60	–

* Values in the brackets are full width at half-maximum (FWHM) in eV.

Table 4
O1s spectra derived oxygen species contents.

Samples	Oxygen species percentage (%)			O_{ads}/O_{lat}
	O_{lat}	O_{ads}	O_{hyd}	
Fresh IO	0.42	0.23	0.35	0.55
Fresh IO-10BA	0.21	0.36	0.42	1.71
IO 20th oxi	0.55	0.21	0.24	0.39
IO 20th red	0.39	0.27	0.34	0.69
IO-10BA 20th oxi	0.56	0.25	0.19	0.45
IO-10BA 20th red	0.39	0.34	0.27	0.88

the surface [50]. The ratio of O_{ads}/O_{lat} can reflect the surface oxygen vacancies for the catalysts. The relative abundance of the three oxygen species on the surface of OCs before and after the redox cycles are listed in Table 4. When freshly calcined, the O_{ads}/O_{lat} of IO-10BA (1.71) was much larger than that of IO (0.55). This indicates the introduction of $BaAl_2O_4$ may possibly increase the oxygen vacancies on the IO surface and then improve its activity. On the other hand, the surface exposure of lattice oxygen from the IO would be reduced due to the surface coverage of the $BaAl_2O_4$, which can also increase the O_{ads}/O_{lat} ratio. After 20 cycles, O_{ads}/O_{lat} for IO-10BA drastically decreased from 1.71 to 0.45, which can be ascribed to the loss of surface $BaAl_2O_4$ due to chemical interaction with the IO or surface abrasion during fluidization. Nevertheless, the O_{ads}/O_{lat} of IO-10BA remained high compared to that of IO after the 20th oxidation (0.39). After the 20th reduction, O_{ads}/O_{lat} increased to 0.69 and 0.88 for IO and IO-10BA, respectively, suggesting the formation of more surface oxygen vacancies as lattice oxygen was consumed. Because of its stronger oxygen transport ability, the reduced IO-10BA exhibited higher O_{ads}/O_{lat} ratio than the reduced IO.

3.3. Discussion

The addition of $BaAl_2O_4$ significantly improved the redox activity and the durability of the IO-based OC, as indicated by the fluidized bed results (Fig. 3 to Fig. 6). The TGA results ubiquitously demonstrated the enhanced oxygen transport capacity of the $BaAl_2O_4$ modified IO (Fig. 10). The lattice oxygen activity was boosted resulting in the enhanced reducibility of the OC as suggested by H_2-TPR shown in Fig. 10 (d). BET and FESEM analyses revealed that the loading of $BaAl_2O_4$ substantially changed the morphological behavior of the OCs. $BaAl_2O_4$ appears to facilitate the accelerated migration of materials within the OC particles, which makes the OC particles much more porous, thus enhancing the intra-particle mass transfer during the redox reaction. Since the OC was repeatedly reduced and oxidized over redox cycles, the ion migration process may influence the state of the solid particles. As discussed above, under reducing environments (such as the ones in FR), $BaAl_2O_4$ can host high concentration of oxygen vacancies as the point defects exist in the structure of $BaAl_2O_4$ [35]. The TGA tests of pure $BaAl_2O_4$ in a CO atmosphere also proved that $BaAl_2O_4$ was seemingly redox active (Fig. 10 (c)) and could participate in the redox reaction as a promoter under a variety of operations conditions, including CO-TGA and H_2-TPR. The increase in oxygen vacancy concentration (in the form of O_{ads}/O_{lat} in Table 4) was also confirmed by the XPS result in this study. A previous report suggested the strong influence of surface oxygen vacancy on the morphology of $BaAl_2O_4$ containing catalysts [35]; this may also be the underlying factor causing the distinct structures of the IO-BA comparing to the unmodified IO. The relative abundance of the oxygen vacancies can remarkably increase the rate of oxygen migration from the bulk to the surface through vacancy-enhanced ionic diffusion [51]. The migration of the bulk lattice oxygen and the iron ions generates more vacancies in the bulk. The coalescence of these vacancies ultimately results in the formation of a highly porous structure [52] inside the particle, as observed from the micrographs of the cross sections of the particles (Fig. 9 B-5 and B-6). During the redox cycles, $BaAl_2O_4$ also migrates into the bulk (as supported by the EDS mapping in Fig. 9 B-5) and interacts with the newly exposed interior surface, which further promotes the formation of more pores inside the particles.

Despite the lack of direct experimental detection, the possible interaction between Fe_2O_3 and $BaAl_2O_4$ cannot be ruled out. According to the recent DFT calculation by Görke et al., the perovskite $BaFeO_3$ is capable of releasing gaseous oxygen and decompose to $Ba_2Fe_2O_5$ [53]. Even though the XRD did not identify the existence of $BaFeO_3$ or $Ba_2Fe_2O_5$, barium ferrite phases produced by the interaction between $BaAl_2O_4$ and Fe_2O_3/Fe_3O_4 may still exist at small quantities. The presence of barium ferrite phases was also suggested by the H_2-TPR profiles of the cycled IO-10BA, which showed H_2 consumption peaks at the low temperature range between 280 and 480 °C. The enhanced oxygen mobility, as a result of phase interactions in the Ba-Fe-Al-O system, was also reported by Wang's group for the chemical looping combustion [53] and reforming [54] of methane. Additionally, during the oxidation step of the OCs, the temperature variation could reach about 40 °C (Figure S5 in SI). The pyroelectric voltage may be generated during this process because of the pyroelectric property of $BaAl_2O_4$ [35,55], which may possibly affect the mobility of the oxygen ions and enhance the oxygen transport ability during the oxidation step. To fully understand the underlying mechanism driving the improvement of the redox performance following $BaAl_2O_4$ doping, the phase interaction in a Ba-Fe-Al-O trimetallic oxides should be systematically investigated in the future. Bridging such knowledge gap would benefit the design of the iron based OCs for a variety of chemical looping processes.

4. Conclusion

The redox performances of iron ore modified by different amounts of $BaAl_2O_4$ were tested for chemical looping combustion of simulated syngas derived from a MSW gasifier. During the 20–50 cycles of redox tests in the fluidized bed reactor, it was found that the reactivity of the iron ore was significantly improved by the doping of 10 wt% of $BaAl_2O_4$. Both XRD and XPS analysis suggested that part of the Fe_2O_3 in IO-10BA can be reduced to FeO. While in the unprocessed iron ore, Fe_2O_3 can only be partially converted to Fe_3O_4. As evidenced by the TGA tests, both the oxygen transport capacity and the reaction rate of

the iron ore were improved remarkably due to the introduction of $BaAl_2O_4$. H_2-TPR tests indicate that the lattice oxygen activity was boosted resulting in the enhanced reducibility of IO-10BA. The additional oxygen vacancies resulted from $BaAl_2O_4$ doping facilitated the rapid oxygen/iron migration during the redox cycles. In addition, the enhanced rate of oxygen ion diffusion also played a role in determining the evolution of the morphologies of OC particles over 50 cycles; the OC particles became much more porous, both on the surface and inside the particle, in the presence of $BaAl_2O_4$. The findings in the present study suggest that the $BaAl_2O_4$-promoted iron ore could be a promising oxygen carrier for CLC, owing to the readily availability of the materials, facile preparation method, and satisfactory redox activity. Nonetheless, the effect of syngas impurities such as HCl and H_2S on the performance of the IO-BA remains to be investigated. Lastly, the detailed phase interaction of Ba-Fe-Al-O system merits further investigation for the rational design of OC materials that can be applied to a variety of chemical looping applications.

Acknowledgement

This research is supported by the National Environment Agency, Ministry of the Environment and Water Resources, Singapore, under the Waste–to–Energy Competitive Research Programme (WTE CRP 1701 105). The authors also acknowledge the management of Nanyang Environment and Water Research Institute and Economic Development Board, Singapore for the support.

Declaration of Competing Interest

We declare that we do not have any commercial or associative interest that represents a conflict of interest in connection with this work.

Appendix A. Supplementary material

Supplementary data to this article can be found online at https://doi.org/10.1016/j.apenergy.2020.115236.

References

[1] Adanez J, Abad A, Garcia-Labiano F, Gayan P, de Diego LF. Progress in chemical-looping combustion and reforming technologies. Prog Energy Combust Sci 2012;38:215–82.
[2] Nandy A, Loha C, Gu S, Sarkar P, Karmakar MK, Chatterjee PK. Present status and overview of chemical looping combustion technology. Renew Sustain Energy Rev 2016;59:597–619.
[3] Metz B, Davidson H, de Coninck M, Meyer L. Special Report on Carbon Dioxide Capture and Storage Prepared by the Working Group III of the Intergovernmental Panel on Climate Change, Cambridge University Press, Cambridge; 2005.
[4] Zhou Z, Han L, Nordness O, Bollas GM. Continuous regime of chemical-looping combustion (CLC) and chemical-looping with oxygen uncoupling (CLOU) reactivity of CuO oxygen carriers. Appl. Catal. B 2015;166–167:132–44.
[5] Mattisson T, Garcia-Labiano F, Kronberger B, Lyngfelt A, Adanez J, Hofbauer H. Chemical-looping combustion using syngas as fuel. Int J Greenhouse Gas Control 2007;1:158–69.
[6] Markstrom P, Linderholm C, Lyngfelt A. Chemical-looping combustion of solid fuels – design and operation of a 100 kW unit with bituminous coal. Int J Greenhouse Gas Control 2013;15:150–62.
[7] Zhao X, Zhou H, Sikarwar VS, Zhao M, Park AHA, Fennell PS, et al. Biomass-based chemical looping technologies: the good, the bad and the future. Energy Environ Sci 2017;10:1885–910.
[8] Adánez J, Abad A, Mendiara T, Gayán P, de Diego LF, García-Labiano F. Chemical looping combustion of solid fuels. Prog. Energy Combust Sci 2018;65:6–66.
[9] Arena U. Process and technological aspects of municipal solid waste gasification. A review. Waste Manage 2012;32:625–39.
[10] Shen Y, Yoshikawa K. Recent progresses in catalytic tar elimination during biomass gasification or pyrolysis—a review. Renew Sustain Energy Rev 2013;21:371–92.
[11] Torres W, Pansare SS, Goodwin JG. Hot gas removal of tars, ammonia, and hydrogen sulfide from biomass gasification gas. Catal Rev 2007;49:407–56.
[12] Chen D, Yin L, Wang H, He P. Reprint of: pyrolysis technologies for municipal solid waste: a review. Waste Manage 2015;37:116–36.
[13] Abdoulmoumine N, Adhikari S, Kulkarni A, Chattanathan S. A review on biomass gasification syngas cleanup. Appl Energy 2015;155:294–307.
[14] Chan WP, Veksha A, Lei J, Oh W-D, Dou X, Giannis A, et al. A hot syngas purification system integrated with downdraft gasification of municipal solid waste. Appl Energy 2019;237:227–40.
[15] Zeng L, Cheng Z, Fan JA, Fan L-S, Gong J. Metal oxide redox chemistry for chemical looping processes. Nat Rev Chem 2018;2:349–64.
[16] Tian H, Simonyi T, Poston J, Siriwardane R. Effect of hydrogen sulfide on chemical looping combustion of coal-derived synthesis gas over bentonite-supported metal-oxide oxygen carriers. Ind Eng Chem Res 2009;48:8418–30.
[17] de Diego LF, García-Labiano F, Adánez J, Gayán P, Abad A, Corbella BM, et al. Development of Cu-based oxygen carriers for chemical-looping combustion. Fuel 2004;83:1749–57.
[18] Cabello A, Dueso C, García-Labiano F, Gayán P, Abad A, de Diego LF, et al. Performance of a highly reactive impregnated Fe_2O_3/Al_2O_3 oxygen carrier with CH_4 and H_2S in a 500Wth CLC unit. Fuel 2014;121:117–25.
[19] Ksepko E, Siriwardane RV, Tian H, Simonyi T, Sciazko M. Effect of H2S on chemical looping combustion of coal-derived synthesis gas over Fe–Mn oxides supported on sepiolite, ZrO_2, and Al_2O_3. Energy Fuels 2012;26:2461–72.
[20] Tan Y, Sun Z, Cabello A, Lu DY, Hughes RW. Effects of H2S on the reactivity of ilmenite ore as chemical looping combustion oxygen carrier with methane as fuel. Energy Fuels 2018;33:585–94.
[21] Leion H, Jerndal E, Steenari B-M, Hermansson S, Israelsson M, Jansson E, et al. Solid fuels in chemical-looping combustion using oxide scale and unprocessed iron ore as oxygen carriers. Fuel 2009;88:1945–54.
[22] Xiao R, Song Q, Song M, Lu Z, Zhang S, Shen L. Pressurized chemical-looping combustion of coal with an iron ore-based oxygen carrier. Combust Flame 2010;157:1140–53.
[23] Gu H, Shen L, Zhong Z, Zhou Y, Liu W, Niu X, et al. Interaction between biomass ash and iron ore oxygen carrier during chemical looping combustion. Chem Eng J 2015;277:70–8.
[24] Shen L, Wu J, Xiao J, Song Q, Xiao R. Chemical-looping combustion of biomass in a 10 kWth reactor with iron oxide as an oxygen carrier. Energy Fuels 2009;23:2498–505.
[25] Abad A, Mendiara T, Gayán P, García-Labiano F, de Diego LF, Bueno JA, et al. Comparative evaluation of the performance of coal combustion in 0.5 and 50 kWth chemical looping combustion units with Ilmenite, Redmud or Iron Ore as oxygen carrier. Energy Procedia 2017;114:285–301.
[26] Haider SK, Azimi G, Duan L, Anthony EJ, Patchigolla K, Oakey JE, et al. Enhancing properties of iron and manganese ores as oxygen carriers for chemical looping processes by dry impregnation. Appl Energy 2016;163:41–50.
[27] Song T, Shen T, Shen L, Xiao J, Gu H, Zhang S. Evaluation of hematite oxygen carrier in chemical-looping combustion of coal. Fuel 2013;104:244–52.
[28] Huang Z, He F, Feng Y, Zhao K, Zheng A, Chang S, et al. Biomass char direct chemical looping gasification using NiO-modified iron ore as an oxygen carrier. Energy Fuels 2013;28:183–91.
[29] Jiang S, Shen L, Wu J, Yan J, Song T. The investigations of hematite-CuO oxygen carrier in chemical looping combustion. Chem. Eng. J. 2017;317:132–42.
[30] Tian X, Zhao H, Ma J. Cement bonded fine hematite and copper ore particles as oxygen carrier in chemical looping combustion. Appl Energy 2017;204:242–53.
[31] Gu H, Shen L, Xiao J, Zhang S, Song T, Chen D. Iron ore as oxygen carrier improved with potassium for chemical looping combustion of anthracite coal. Combust. Flame 2012;159:2480–90.
[32] Gu H, Shen L, Zhong Z, Niu X, Liu W, Ge H, et al. Cement/CaO-modified iron ore as oxygen carrier for chemical looping combustion of coal. Appl Energy 2015;157:314–22.
[33] Xie X, Li Y, Wang W, Shi L. HCl removal using cycled carbide slag from calcium looping cycles. Appl Energy 2014;135:391–401.
[34] Stemmler M, Tamburro A, Muller M. Laboratory investigations on chemical hot gas cleaning of inorganic trace elements for the “UNIQUE" process, Fuel, 2013;108:31–36.
[35] Zhang LW, Wang L, Zhu YF. Synthesis and performance of $BaAl_2O_4$ with a wide spectral range of optical absorption. Adv Funct Mater 2007;17:3781–90.
[36] Kaur J, Jaykumar B, Dubey V, Shrivastava R, Suryanarayana NS. Optical properties of rare earth-doped barium aluminate synthesized by different methods-a review. Res Chem Intermed 2013;41:2317–43.
[37] Pandey A, Chithambo ML. Thermoluminescence of the persistent-luminescence phosphor, $BaAl_2O_4$; a stuffed tridymite. Radiat Measur 2018;120:73–7.
[38] Liu W, Dennis JS, Scott SA. The effect of addition of ZrO_2 to Fe_2O_3 for hydrogen production by chemical looping. Ind. Eng. Chem. Res. 2012;51:16597–609.
[39] Liu W, Lim JY, Saucedo MA, Hayhurst AN, Scott SA, Dennis JS. Kinetics of the reduction of wüstite by hydrogen and carbon monoxide for the chemical looping production of hydrogen. Chem Eng Sci 2014;120:149–66.
[40] Newsome DS. The water-gas shift reaction. Catal Rev Sci Eng 1980;21:275–318.
[41] Adánez J, Cuadrat A, Abad A, Gayán P, de Diego LF, García-Labiano F. Ilmenite activation during consecutive redox cycles in chemical-looping combustion. Energy Fuels 2010;24:1402–13.
[42] Xian H, Zhang X, Li X, Li L, Zou H, Meng M, et al. $BaFeO_{3-x}$ perovskite: An efficient NO_x absorber with a high sulfur tolerance. J. Phys. Chem. C 2010;114:11844–52.
[43] Ciambelli P, Cimino S, De Rossi S, Lisi L, Minelli G, Porta P, et al. $AFeO_3$ (A = La, Nd, Sm) and $LaFe_{1-x}Mg_xO_3$ perovskites as methane combustion and CO oxidation catalysts: structural, redox and catalytic properties. Appl. Catal. B 2001;29:239–50.
[44] Rousseau S, Loridant S, Delichere P, Boreave A, Deloume J, Vernoux P. La (1–x) SrxCo1 − yFeyO3 perovskites prepared by sol–gel method: characterization and relationships with catalytic properties for total oxidation of toluene. Appl. Catal. B 2009;88:438–47.
[45] Huang J, Liu W, Yang Y. Phase interactions in Mg-Ni-Al-O oxygen carriers for chemical looping applications. Chem. Eng. J. 2017;326:470–6.
[46] Siriwardane R, Riley J, Tian H, Richards G. Chemical looping coal gasification with calcium ferrite and barium ferrite via solid–solid reactions. Appl Energy

2016;165:952–66.
[47] Huang F, Tian M, Zhu Y, Wang X, Wang A, Li L, et al. Fe-substituted Ba-hexaaluminate with enhanced oxygen mobility for CO2 capture by chemical looping combustion of methane. J Energy Chem 2019;29:50–7.
[48] Grosvenor AP, Kobe BA, Biesinger MC, McIntyre NS. Investigation of multiplet splitting of Fe 2p XPS spectra and bonding in iron compounds. Surf Interface Anal 2004;36:1564–74.
[49] Zheng Y, Li K, Wang H, Tian D, Wang Y, Zhu X, et al. Designed oxygen carriers from macroporous $LaFeO_3$ supported CeO_2 for chemical-looping reforming of methane. Appl Catal B 2017;202:51–63.
[50] Yang X, Sun H, Zhang L, Zhao L, Lian J, Jiang Q. High efficient photo-fenton catalyst of alpha-Fe_2O_3/MoS_2 hierarchical nanoheterostructures: reutilization for supercapacitors. Sci Rp. 2016;6:31591.
[51] Zhu Y, Liu R, Sun X, Ma X, Wang X, Tian H. Metal modified hexaaluminates for syngas generation and CO_2 utilization via chemical looping. Int. J. Hydrogen Energy 2019;44:10218–31.
[52] Knutsson P, Linderholm C. Characterization of ilmenite used as oxygen carrier in a 100 kW chemical-looping combustor for solid fuels. Appl Energy 2015;157:368–73.
[53] Görke R, Hu W, Dunstan M, Dennis J, Scott S. Exploration of the material property space for chemical looping air separation applied to carbon capture and storage. Appl Energy 2018;212:478–88.
[54] Shen Q, Huang F, Tian M, Zhu Y, Li L, Wang J, et al. Effect of regeneration period on the selectivity of synthesis gas of Ba-hexaaluminates in chemical looping partial oxidation of methane. ACS Catal 2018;9:722–31.
[55] Xie C, Zeng Q, Dong D, Gao S, Cai Y, Oganov AR. First-principles calculations of the dielectric and vibrational properties of ferroelectric and paraelectric $BaAl_2O_4$. Phys. Lett. A 2014;378:1867–70.